Poro-mechanical analysis of a structural battery electrolyte: Experimental study and model calibration

Mechanics of Materials 216 (2026) 105632

Contents lists available at ScienceDirect

Mechanics of Materials

journal homepage: www.elsevier.com/locate/mecmat

Research paper

Poro-mechanical analysis of a structural battery electrolyte: Experimental study and model calibration

Carl Larsson *, Fredrik Larsson, Ruben Tavano, Johanna Xu, Kenneth Runesson, Leif E. Asp

Department of Mechanical Engineering, Chalmers University of Technology, Gothenburg, SE-412 96, Sweden

ARTICLE INFO

Keywords:
Computational mechanics
Experimental mechanics
Viscoelasticity
Porous media
Model calibration
Coupled problems

ABSTRACT

We present the calibration and validation of a continuum poro-viscoelastic model for a structural battery electrolyte in the finite deformation setting. The model is based on a Maxwell type rheology incorporating a Norton evolution law, coupled with a simple Darcy type seepage formulation to describe fluid transport. Experiments were performed using in-house manufactured cylindrical specimens subjected to uniaxial compression at different strain rates. Radial deformation of the specimens was recorded using an optical camera, while mass measurements before and after compression were used to quantify liquid electrolyte seepage. The experimental data were used to calibrate the model. Furthermore, independent stress relaxation tests conducted at varying strain rates were used for validation.

The proposed model successfully captures the rate-dependent stress–strain behaviour, radial extension, and associated mass loss due to seepage, particularly at large compressive strains. Some discrepancies remain in the representation of time dependent relaxation at higher strain rates. The framework provides a robust foundation for describing coupled solid–fluid interaction in structural battery electrolytes and supports future efforts towards micromechanical modelling and design optimization of multifunctional energy storing composites.

1. Introduction

Structural battery composites are multifunctional materials that simultaneously serve as energy storage device and construction material. The multifunctionality is enabled by carbon fibres, which act both as structural reinforcement and as electrodes due to their turbostratic graphitic microstructure. Chaudhary et al. (2024) demonstrated the most recent structural battery composite by embedding carbon fibre electrodes in a nano-porous structural battery electrolyte (SBE). Unlike conventional lithium-ion batteries that utilize liquid or gel-based electrolytes, structural batteries require a solid phase with sufficient stiffness to transfer mechanical loads between the carbon fibres.

The first generation of such a biphasic electrolyte was developed by Ihrner et al. (2017), consisting of a solid matrix based on bisphenol A dimethacrylate monomer and organic liquid electrolyte filled pores, containing lithium trifluoromethanesulfonate (LiTFS). The two phases were initially mixed in a solution and then polymerized through UV curing. Upon curing, a nano-porous percolating network is formed, where the solid phase stiffens and provides mechanical integrity, while the liquid phase enables ion transport. Even though very promising, the use of UV curing is not feasible on multi-layered structural battery composites due to the non-transparent nature of the constituents. For this reason, heat curing was proposed by Schneider et al. (2019). The same polymerization induced phase separation was achieved with comparable ionic conductivities and slightly larger pores. The mechanical properties were almost identical with an increased storage modulus at higher temperatures for heat cured samples compared to UV cured ones.

Duan et al. (2023) demonstrated that these liquid filled pores are uniformly distributed, resulting in isotropic material properties such as ionic conductivity, elastic modulus and Poisson's ratio. Furthermore, more than 99% of the pores form a connected network. However, the predicted ionic conductivity was overestimated by the computational models, likely due to resolution limits that exclude pores smaller than 10 nm. In a more recent study, Cattaruzza et al. (2023) further investigated the relation between the microstructure and the ionic conductivity in thermally-cured SBEs. For the first time, pores in the nanoscale size range were identified and the ionic conductivity was precisely measured to be $2.9 \cdot 10^{-4}$ S/cm for a 50/50 monomer to liquid electrolyte weight ratio. Furthermore, they explained the measured values of ionic conductivity by studying the diffusion and the

* Corresponding author.
E-mail address: calar@chalmers.se (C. Larsson).

https://doi.org/10.1016/j.mechmat.2026.105632
Received 10 November 2025; Received in revised form 27 January 2026; Accepted 3 February 2026
Available online 12 February 2026

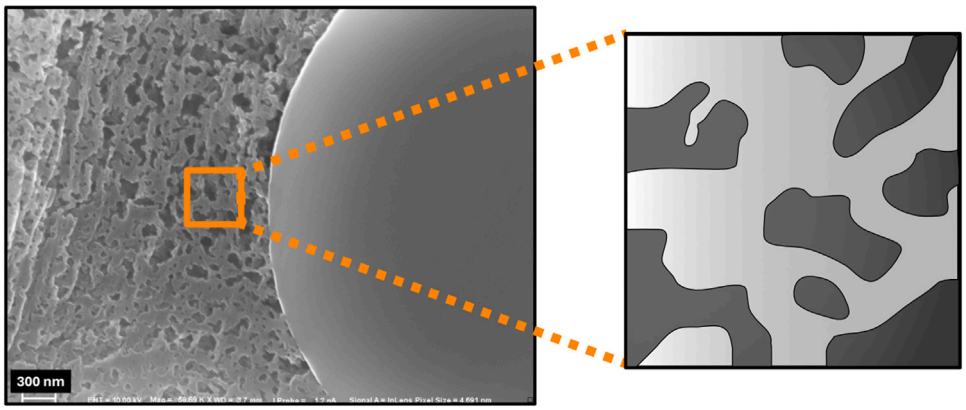

Fig. 1. SEM image of a structural battery negative electrode cross section. A carbon fibre embedded in the structural battery electrolyte matrix, and a zoom-in schematic representation highlighting the fluid (dark-grey) and solid (light-grey) domains.

mobility of the solvent and lithium bis(trifluoromethanesulfonyl)imide (LiTFSI) in the solid part of the SBE, showing that the transport in this region is also of significant importance. Additional mechanical characterization by Tavano et al. (2024) on a similar composition of SBE as Schneider et al. (2019), showed that the SBE has an elastic modulus of 412 MPa and a Poisson's ratio of 0.34, with failure strains of 28.1% in compression and 2.49% in tension, respectively. These tests were conducted at a displacement rate of 0.5 mm/min, corresponding to approximately 1.8% strain per minute for the tensile specimens. The large measured failure strain in compression allows for operation at large compressive strains, which motivates modelling based on finite deformation kinematics.

The nano-porous structure of the SBE is depicted in Fig. 1. It appears that the cured SBE exhibits a fine-scale porous structure, with light grey regions indicating the solid phase and dark grey regions representing the interconnected liquid electrolyte-filled pores.

Lithiation of carbon fibres is known to induce anisotropic expansion, generating local internal stresses within the structural electrolyte matrix (Duan et al., 2021). Previous models by Larsson et al. (2023, 2025), overestimate these stresses, partly due to the use of simplified neo-Hookean material models and lack of experimental data. Moreover, Pipertzis et al. (2025) observed that the effective ionic conductivity over the carbon fibre electrode increases after lithiation-delithiation cycles, which we can interpret as an indication that damage occurs in the electrolyte. This formation of damage is most likely due to local crushing of the SBE, caused by the expansion of the fibres, although this mechanism has not been definitively confirmed. Consequently, it is thought that additional ion transport pathways are formed. To better understand the damage mechanisms and structural integrity of the SBE, it is essential to investigate its behaviour under various mechanical loading conditions, particularly in compression.

In order to obtain experimental data that can be used for calibration of the constitutive models, we manufactured cylindrical specimens and subjected them to compressive mechanical loading at different strain rates. To solve the appropriate inverse problem, we model the experiments by employing a continuum-based porous media theory that involves quasi-static equilibrium and fluid mass balance in the finite deformation setting. In this way, we are able to capture stress assisted fluid transport. Whereas some experimental data are used for calibration of the computational models, others are used for model validation. Although the prime use of models for the large deformation regime is the structural battery, such models are highly relevant also for electro-chemically activated shape-forming devices (sensors and actuators) (Johannisson et al., 2020; Carlstedt et al., 2023).

2. Experimental method

2.1. Materials

The SBE samples consisted of a 50:50 weight ratio of monomer and liquid electrolyte. The monomer consisted of bisphenol-A ethoxylate dimethacrylate (BPMA) mixed with a $2,2'$-azobis (2-methylpropionitrile) (AIBN) thermal initiator. A 1% weight relative to the monomer of thermal initiator was used. The liquid electrolyte (LE) was made from a 1.0 M solution of lithium bis(trifluoromethanesulfonyl)imide (LiTFSI) salt dissolved in a mixture of ethylene carbonate (EC) and propylene carbonate (PC) (Canrud, 2025). The two carbonates were mixed in a 1:1 weight ratio. All the materials were stored inside a glovebox to ensure no significant contact with moisture and oxygen. Furthermore, a pre-mixed electrolyte mixture was used for some of the specimens. All materials were used as received.

To manufacture the compression samples, the same technique described by Tavano et al. (2024) was used. Cylindrical samples with approximately 2:1 ratio of length to diameter were obtained and the two end surfaces were polished to ensure flat and parallel surfaces. A nominal length and diameter of 24 mm and 12 mm was achieved, respectively.

2.2. Compression tests

The mechanical tests followed the ASTM D695 standard. The samples were tested using an Instron 5500R tensile tester paired with a 100 kN load cell. Flat parallel stiff platens were used to apply the axial load in order to investigate the rate dependence on the mechanical response. Deformation during the compression test was measured from the displacement of the top cross head. Speckle patterning in combination with DIC could not be applied due to liquid seepage from the sample at high strain values (Tavano et al., 2024). An initial compressive preload was applied up to 50 N, after which, the compression test was performed until a certain predefined top displacement was reached. The unloading response was also monitored until the recorded cross-head force reached 0 N.

Furthermore, the effect of loading rate on the diameter evolution at the mid-height of the sample was investigated. A 48 megapixel optical camera was used to capture a series of frontal images of the compression samples. A resolution of 4032 × 3024 pixels was considered with a 13 mm focal length and an $f2.2$ aperture. The obtained images were analysed with the ImageJ software so that the diameter values could be measured; subsequently, the diameter evolution could be obtained.

2.3. Mass loss tests

The loss of fluid mass suffered during the compression tests was measured using a Radwag X7 laboratory scale. The pristine samples were weighed before and after compression, and the difference represents the loss of fluid mass that seeped out through the boundaries.

2.4. Relaxation tests

The stress relaxation tests followed the ASTM D2990-17 standard, with varying relaxation times. The same type of polymeric cylindrical samples used for the compression tests as employed to ensure direct comparability of the mechanical behaviour. Each specimen was compressed at a given rate to a prescribed position of the end platens, which were then kept in position for the duration of the relaxation test, during which a decay in compressive stress was continuously recorded. Once the stress relaxation test was completed, the sample was unloaded and weighed to record the loss of mass. Like the compression tests, an initial preload of 50 N was applied to ensure consistent contact between the sample and the platens.

3. Model description

3.1. Preliminaries

To represent the experimental tests described in the previous section, we adopt a model that describes the time- and rate-dependent mechanical response of a fluid-saturated porous body undergoing arbitrarily large (finite) deformations. The key ingredient is a model of visco-hyperelasticity to characterize the solid skeleton together with a quite simple model of the Darcy-type to describe seepage. A rich literature exists on the quasistatic, finite deformation, response of porous media. Among important contributions we merely mention (Sanavia et al., 2002; Schrefler, 2002; Ehlers, 2018). A review of various modelling attempts is given by (De Boer, 2012).

In the context of structural batteries, Carlstedt et al. investigated how stress-induced seepage affects ion mobility in a structural battery electrolyte (Carlstedt et al., 2022). In that work, which was restricted to small strain kinematics, effective poro-elastic properties were obtained upon calibration of analytical (Bruggeman) models against data from virtual material tests. The virtual data were generated using artificially constructed idealized representative volume elements (RVEs) as proposed by Tu et al. (2020). However, as discussed by Duan et al. (2023), Pipertzis et al. (2023), measurements indicate broad pore size distributions and the presence of closed pores. These observations call into question the representativeness of such artificial RVEs, the resulting virtual data and consequently, the calibrated poro-elastic properties.

The deformation gradient $\boldsymbol{F}$ is expressed as $\boldsymbol{F} := \boldsymbol{I} + \boldsymbol{u} \otimes \boldsymbol{\nabla}_{\mathrm{X}}$, where $\boldsymbol{I}$ is the (2nd order) identity tensor, $\boldsymbol{u}$ is the displacement field, $\boldsymbol{\nabla}_{\mathrm{X}}$ is the differential operator with respect to the reference configuration. Moreover, we introduce the so-called "effective" 1st Piola–Kirchhoff (PK) stress $\boldsymbol{P}'$, defined as

$$\boldsymbol{P}' = \boldsymbol{P} + pJ\boldsymbol{F}^{-\mathrm{T}}, \tag{1}$$

where $\boldsymbol{P}$ is the total 1st PK stress,[1] p is the fluid pore pressure, and $J = \det(\boldsymbol{F})$ is the volume ratio of deformed to undeformed unit volume.

[1] We remark that the definition of effective stress is not unique; rather, the present choice corresponds to the classical definition by Terzaghi et al. (1996), cf., discussion by Ehlers (2018).

3.2. Balance equations - Boundary conditions - Weak forms

The relevant balance equations are (i) balance of linear momentum and (ii) balance of fluid mass. For the quasi-static problem it is then sufficient to choose the pair $(\boldsymbol{u}, p)$ as the independent fields. At the outset, we consider the general setting in 3D without a priori introducing constraints from geometric and material symmetry. Ignoring self-weight and assuming quasi-static conditions, we then state the relevant initial–boundary-value problem in $\Omega \times (0, T]$ as follows:

$$-\boldsymbol{P} \cdot \boldsymbol{\nabla}_{\mathrm{X}} = \boldsymbol{0}, \tag{2a}$$

$$\dot{\boldsymbol{\Phi}} + \left[\rho^{\mathrm{F}} \phi \boldsymbol{W}\right] \cdot \boldsymbol{\nabla}_{\mathrm{X}} = 0, \tag{2b}$$

where $\boldsymbol{W}$ is the seepage velocity, ϕ is the current porosity. $\boldsymbol{\Phi}$ is the fluid (mass) storage function, defined as

$$\boldsymbol{\Phi} := J\phi\rho^{\mathrm{F}}, \tag{3}$$

and where ρ^{F} is the current density of the fluid.

As to the appropriate choice of boundary conditions, we first consider a generic boundary part with outwards pointing unit normal $\boldsymbol{N}$. We then introduce the normal displacement $u_{\mathrm{n}} := \boldsymbol{u} \cdot \boldsymbol{N}$, the tangential displacement (vector) $\boldsymbol{u}_{\mathrm{t}} := \boldsymbol{u} - u_{\mathrm{n}}\boldsymbol{N}$. Similarly, we define the normal seepage $W_{\mathrm{n}} := \boldsymbol{W} \cdot \boldsymbol{N}$. Furthermore, we define the traction $\boldsymbol{t} := \boldsymbol{P} \cdot \boldsymbol{N}$, the normal traction $t_{\mathrm{n}} := \boldsymbol{t} \cdot \boldsymbol{N}$ and the tangential traction $\boldsymbol{t}_{\mathrm{t}} := \boldsymbol{t} - t_{\mathrm{n}}\boldsymbol{N}$.

For the cylindrical specimen, let Γ_{T}, Γ_{B}, Γ_{P} denote the top, bottom and perimeter surfaces, respectively, as shown in Fig. 2. We shall then define two different loading-conditions with respect to the choice of boundary conditions on $\Gamma_{\mathrm{T/B}}$, which are either *smooth* or *rough*. The smooth case represents frictionless boundaries while the counterpart rough represents maximized friction, i.e., full sticking. We then choose (D = Dirichlet, N = Neumann) the conditions

$$u_{\mathrm{n}} = u^{\mathrm{T/B}}_{\mathrm{app}} \text{ (D)}, \quad W_{\mathrm{n}} = 0 \text{ (N)} \quad \text{on} \quad \Gamma_{\mathrm{T/B}} \tag{4a}$$

$$\boldsymbol{t} = \boldsymbol{0} \quad \text{(N)}, \quad p = 0 \text{ (D)} \quad \text{on} \quad \Gamma_{\mathrm{P}} \tag{4b}$$

$$\boldsymbol{t}_{\mathrm{t}} = \boldsymbol{0} \quad \text{(N)} \quad \text{on} \quad \Gamma_{\mathrm{T/B}} \text{ (smooth)} \tag{4c}$$

$$\boldsymbol{u}_{\mathrm{t}} = \boldsymbol{0} \quad \text{(D)} \quad \text{on} \quad \Gamma_{\mathrm{T/B}} \text{ (rough)} \tag{4d}$$

Here, $u^{\mathrm{T/B}}_{\mathrm{app}}$ denotes the prescribed normal (vertical) displacement component on the boundary parts $\Gamma_{\mathrm{T/B}}$. In practise, the prescribed normal displacement $u^{\mathrm{B}}_{\mathrm{app}} = 0$. Obviously, the entire displacement $\boldsymbol{u}$, is prescribed on $\Gamma_{\mathrm{T/B}}$ in the case of a rough boundary, whereas only the normal component is prescribed when the boundary is smooth.

The time-continuous weak forms, corresponding to the balance equations in Eqs. (2a) and (2b), read: Find $\boldsymbol{u}(\boldsymbol{x}, t)$, $p(\boldsymbol{x}, t) \in \mathbb{U} \times \mathbb{P}$ that solve

$$\int_{\Omega} \boldsymbol{P} : \left[\delta\boldsymbol{u} \otimes \boldsymbol{\nabla}_{\mathrm{X}}\right] \mathrm{d}\Omega = 0, \tag{5a}$$

$$\int_{\Omega} \dot{\boldsymbol{\Phi}}\delta p \mathrm{d}\Omega - \int_{\Omega} \rho^{\mathrm{F}}\phi\boldsymbol{W} \cdot \left[\boldsymbol{\nabla}_{\mathrm{X}}\delta p\right] \mathrm{d}\Omega = 0, \tag{5b}$$

that must hold for appropriately chosen test functions $\delta\boldsymbol{u}$, $\delta p \in \mathbb{U}^0 \times \mathbb{P}^0$.

For a smooth boundary $\Gamma_{\mathrm{T/B}}$, the trial and test set for displacements are given as

$$\mathbb{U} = \left\{ \boldsymbol{u}' \text{ suff. regular on } \Omega\text{: } u'_{\mathrm{n}} = u^{\mathrm{T/B}}_{\mathrm{app}} \text{ on } \Gamma_{\mathrm{T/B}} \right\}, \tag{6a}$$

$$\mathbb{U}^0 = \left\{ \boldsymbol{u}' \text{ suff. regular on } \Omega\text{: } u'_{\mathrm{n}} = 0 \text{ on } \Gamma_{\mathrm{T/B}} \right\}, \tag{6b}$$

whereas for a rough boundary $\Gamma_{\mathrm{T/B}}$

$$\mathbb{U} = \left\{ \boldsymbol{u}' \text{ suff. regular: } u'_{\mathrm{n}} = u^{\mathrm{T/B}}_{\mathrm{app}},\ \boldsymbol{u}'_{\mathrm{t}} = \boldsymbol{0} \text{ on } \Gamma_{\mathrm{T/B}} \right\}, \tag{7a}$$

$$\mathbb{U}^0 = \left\{ \boldsymbol{u}' \text{ suff. regular: } \boldsymbol{u}' = \boldsymbol{0} \text{ on } \Gamma_{\mathrm{T/B}} \right\}. \tag{7b}$$

Finally, the trial and test space for the pressure is chosen as

$$\mathbb{P} = \left\{ p' \text{ suff. regular: } p' = 0 \text{ on } \Gamma_{\mathrm{P}} \right\} = \mathbb{P}^0. \tag{8}$$

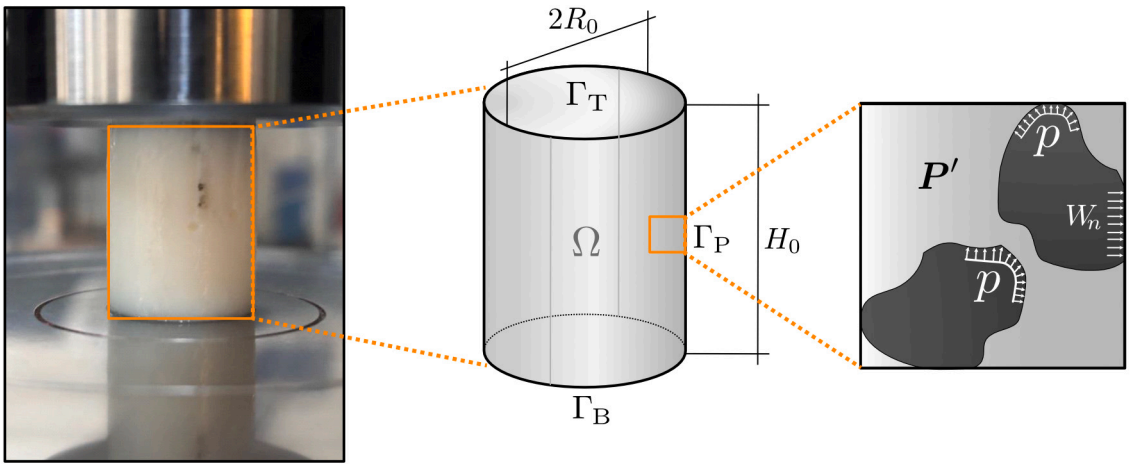

Fig. 2. Cylindrical SBE specimen subjected to compressive deformation (left figure), illustration of the domain Ω, along with the top boundary Γ_T, bottom boundary Γ_B and perimeter boundary Γ_P (middle figure), schematic illustration of the nano-porous structure with pore pressure field p, normal seepage W_n and the effective 1st PK stress in the solid skeleton $\boldsymbol{P}'$ (right figure).

3.3. Constitutive equations

The drained solid skeleton is represented as a viscoelastic material. The constitutive relation is formulated in terms of the effective 2nd PK stress $\boldsymbol{S}'$, which is related to the effective 1st PK stress through

$$\boldsymbol{P}'(\boldsymbol{F}, \boldsymbol{F}_v) = \boldsymbol{F} \cdot \boldsymbol{S}'(\boldsymbol{C}, \boldsymbol{C}_{el}). \tag{9}$$

The rheological basis is the so-called three-parameter model with two chains, as illustrated in Fig. 3. A similar model for finite viscoelasticity, motivated by the dissipation inequality and involving an intermediate viscous configuration, was proposed by Reese and Govindjee (1998). Extensions of poro-viscoelastic models for soft biological tissues have also been developed by Ehlers and Markert (2001).

The total volume specific strain energy density is additively decomposed into equilibrium and non-equilibrium contributions, associated with the equilibrium spring and the spring–dashpot branch, respectively; hence,

$$\psi = \psi^{EQ} + \psi^{NEQ}. \tag{10}$$

Since the equilibrium response is purely elastic, we conveniently parametrize $\psi^{EQ} = \psi^{EQ}(\boldsymbol{C})$, where $\boldsymbol{C} = \boldsymbol{F}^T \cdot \boldsymbol{F}$ is the right Cauchy–Green deformation. For the non-equilibrium branch, the deformation gradient $\boldsymbol{F}$ is multiplicatively decomposed into an elastic part $\boldsymbol{F}_{el}$ associated with the spring, and a viscous part $\boldsymbol{F}_v$ representing the dashpot deformation, so that $\boldsymbol{F} = \boldsymbol{F}_{el} \cdot \boldsymbol{F}_v$. The non-equilibrium contribution to the strain energy density therefore depends on the elastic measure as $\psi^{NEQ} = \psi^{NEQ}(\boldsymbol{C}_{el})$, where the elastic right Cauchy–Green tensor is given by $\boldsymbol{C}_{el} = \boldsymbol{F}_{el}^T \cdot \boldsymbol{F}_{el} = \boldsymbol{F}_v^{-T} \cdot \boldsymbol{C} \cdot \boldsymbol{F}_v^{-1}$.

Finally, we specify the constitutive forms of the strain energy density functions for both the equilibrium and non-equilibrium branches using a neo-Hookean formulation. The energy contribution of the equilibrium spring, accounting for both isochoric and volumetric deformations, is given by

$$\psi^{EQ}(\boldsymbol{C}) = \frac{\mu_1}{2}\left[J^{-2/3}\,\mathrm{tr}(\boldsymbol{C}) - 3\right] + \frac{\kappa_1}{2}\left[J - 1\right]^2, \tag{11}$$

where $J = \sqrt{\det(\boldsymbol{C})}$ is the volume ratio of the total deformation, μ_1 and κ_1 are the bulk and shear moduli of the equilibrium spring, respectively. For the non-equilibrium (viscoelastic) chain, only the isochoric part is considered to neglect viscous resistance to volumetric changes. The corresponding energy density is therefore expressed as

$$\psi^{NEQ}(\boldsymbol{C}_{el}) = \frac{\mu_2}{2}\left[J_{el}^{-2/3}\,\mathrm{tr}(\boldsymbol{C}_{el}) - 3\right], \tag{12}$$

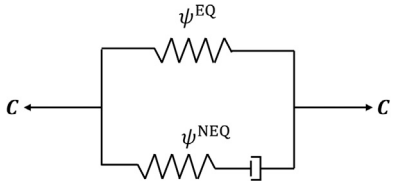

Fig. 3. Rheological visualization of the material model for the solid drained skeleton: The top chain represents the static response, i.e., the rate-independent spring. The bottom chain represents the dynamic response, a spring and a viscous dashpot.

where $J_{el} = \sqrt{\det(\boldsymbol{C}_{el})}$ denotes the elastic volume ratio and μ_2 is the shear modulus associated with the non-equilibrium branch. The effective second Piola–Kirchhoff stress can thus be written as

$$\boldsymbol{S}' = 2\frac{\partial \psi}{\partial \boldsymbol{C}} = 2\left[\frac{\partial \psi^{EQ}}{\partial \boldsymbol{C}} + \frac{\partial \psi^{NEQ}}{\partial \boldsymbol{C}_{el}} : \frac{\partial \boldsymbol{C}_{el}}{\partial \boldsymbol{C}}\right]. \tag{13}$$

In the intermediate configuration, the viscous response is governed by a Norton type evolution law for the viscous velocity gradient,

$$\boldsymbol{l}_v = \dot{\boldsymbol{F}}_v \cdot \boldsymbol{F}_v^{-1}, \tag{14}$$

which is expressed as

$$\boldsymbol{l}_v = \frac{1}{t_*}\left[\frac{M_v^e}{\sigma_0}\right]^n \frac{3}{2}\frac{\boldsymbol{M}_{v,d}}{M_v^e}. \tag{15}$$

Here, a power law dependence on the equivalent driving stress is introduced to capture (rate-dependent) viscous effects. The evolution law is driven by the Mandel stress tensor

$$\boldsymbol{M}_v = \boldsymbol{C}_{el} \cdot 2\frac{\partial \psi^{NEQ}}{\partial \boldsymbol{C}_{el}}, \tag{16}$$

with volumetric and deviatoric components expressed as

$$M_{v,vol} = \frac{1}{3}\,\mathrm{tr}(\boldsymbol{M}_v), \quad \boldsymbol{M}_{v,d} = \boldsymbol{M}_v - M_{v,vol}\,\boldsymbol{I}. \tag{17}$$

The equivalent Mandel stress is defined in the usual manner as

$$M_v^e = \sqrt{\frac{3}{2}\,\boldsymbol{M}_{v,d} : \boldsymbol{M}_{v,d}}. \tag{18}$$

The material parameters t_*, n, and σ_0 govern the viscous evolution. Specifically, t_* is the relaxation time, n is the Norton exponent controlling stress sensitivity, and σ_0 is the reference stress.

In the current model, we shall assume that the solid phase is incompressible so that the solid phase density is constant $\rho^s = \rho_0^s$,

while compressibility is introduced in the fluid phase. This assumption effectively reduces the parameter space and omits solid phase density dependence with respect to pore pressure and mechanical deformation. Based on this assumption, the current porosity can be expressed as

$$\phi(J) = 1 - \frac{1}{J}[1 - \phi_0], \tag{19}$$

where ϕ_0 is the initial (undeformed) porosity.

Furthermore, the constitutive relation for the pore fluid density is assumed to follow a linear compressibility law,

$$\rho^{\mathrm{F}}(p) = \rho_0^{\mathrm{F}}\left[1 + \frac{p}{\kappa^{\mathrm{F}}}\right], \tag{20}$$

where κ^{F} denotes the intrinsic bulk modulus of the fluid. In this form, the density increases linearly with pore pressure relative to the initial fluid density ρ_0^{F}. For the fluid flux, we adopt a Darcy type law in the reference configuration. The relative seepage velocity scaled by the current porosity as the constitutive quantity gives

$$\phi \boldsymbol{W} = -\boldsymbol{K} \cdot \boldsymbol{\nabla}_{\mathrm{X}} p, \tag{21}$$

where $\boldsymbol{K}$ is the permeability tensor in the reference configuration. In the present study, the permeability is assumed macroscopically isotropic, such that $\boldsymbol{K} = K\boldsymbol{I}$.

4. Axisymmetric representation at the experimental setup

4.1. Preliminaries - Kinematics - Weak forms

For convenience, the analysis is performed in an axisymmetric representation of the cylindrical specimens, whereby polar coordinates (r, θ, z) are used in the reference (undeformed) configuration $\Omega = \bar{\Omega} \times [0, 2\pi]$ with $\bar{\Omega} = [0, R_0] \times [0, H_0]$ representing the computational domain with related surfaces $\bar{\Gamma}_{\mathrm{T/B}}$ and $\bar{\Gamma}_{\mathrm{R}}$. The corresponding set of unit orthonormal base vectors are $(\boldsymbol{e}_r, \boldsymbol{e}_\theta, \boldsymbol{e}_z)$. The displacement vector $\boldsymbol{u}$ is then represented as

$$\boldsymbol{u} = u_r \boldsymbol{e}_r + u_z \boldsymbol{e}_z \tag{22}$$

where it is used that $u_\theta = 0$ (due to axisymmetry). Further, we consider the case where the applied displacement on the bottom boundary $u^{\mathrm{B}}_{\mathrm{app}} = 0$ and the top boundary $u^{\mathrm{T}}_{\mathrm{app}} = -\epsilon(t)z$, where $\epsilon(t)$ is the relevant prescribed deformation. The gradient operator $\boldsymbol{\nabla}_{\mathrm{X}}$ has the representation

$$\boldsymbol{\nabla}_{\mathrm{X}} = \boldsymbol{e}_r \frac{\partial}{\partial r} + \boldsymbol{e}_\theta \frac{1}{r}\frac{\partial}{\partial \theta} + \boldsymbol{e}_z \frac{\partial}{\partial z}. \tag{23}$$

Upon using the constraints $\frac{\partial u_r}{\partial \theta} = \frac{\partial u_z}{\partial \theta} = 0$ and $\frac{\partial p}{\partial \theta} = 0$ we obtain, in standard fashion, that $\boldsymbol{F} = \boldsymbol{I} + \boldsymbol{H}$ with

$$\boldsymbol{H} := \boldsymbol{u} \otimes \boldsymbol{\nabla}_{\mathrm{X}} = \frac{\partial u_r}{\partial r}\boldsymbol{e}_r \otimes \boldsymbol{e}_r + \frac{\partial u_r}{\partial z}\boldsymbol{e}_r \otimes \boldsymbol{e}_z + \frac{1}{r}u_r \boldsymbol{e}_\theta \otimes \boldsymbol{e}_\theta + \frac{\partial u_z}{\partial r}\boldsymbol{e}_z \otimes \boldsymbol{e}_r + \frac{\partial u_z}{\partial z}\boldsymbol{e}_z \otimes \boldsymbol{e}_z \tag{24}$$

and

$$\boldsymbol{\nabla}_{\mathrm{X}} p = \frac{\partial p}{\partial r}\boldsymbol{e}_r + \frac{\partial p}{\partial z}\boldsymbol{e}_z. \tag{25}$$

The corresponding (time-continuous) weak forms are obtained as special cases of Eqs. (5a) and (5b) as follows: Upon choosing, in turn, for $\delta u_r \neq 0$ ($\delta u_z = 0$)

$$\delta \boldsymbol{u} \otimes \boldsymbol{\nabla}_X = \frac{\partial \delta u_r}{\partial r}\boldsymbol{e}_r \otimes \boldsymbol{e}_r + \frac{\partial \delta u_r}{\partial z}\boldsymbol{e}_r \otimes \boldsymbol{e}_z + \frac{1}{r}\delta u_r \boldsymbol{e}_\theta \otimes \boldsymbol{e}_\theta, \tag{26}$$

in Eq. (5a), for $\delta u_z \neq 0$ ($\delta u_r = 0$)

$$\delta \boldsymbol{u} \otimes \boldsymbol{\nabla}_X = \frac{\partial \delta u_z}{\partial r}\boldsymbol{e}_z \otimes \boldsymbol{e}_r + \frac{\partial \delta u_z}{\partial z}\boldsymbol{e}_z \otimes \boldsymbol{e}_z, \tag{27}$$

in Eq. (5a), and for $\delta p \neq 0$

$$\boldsymbol{\nabla}_{\mathrm{X}} \delta p = \frac{\partial \delta p}{\partial r}\boldsymbol{e}_r + \frac{\partial \delta p}{\partial z}\boldsymbol{e}_z \tag{28}$$

in Eq. (5b), we seek $u_r(r, z, t) \in \mathbb{U}_r$, $u_z(r, z, t) \in \mathbb{U}_z$, $p(r, z, t) \in \mathbb{P}$ that satisfy

$$\int_{\bar{\Omega}} \left[P_{rr}\frac{\partial \delta u_r}{\partial r} + P_{rz}\frac{\partial \delta u_r}{\partial z} + P_{\theta\theta}\frac{1}{r}\delta u_r\right] r \mathrm{d}\bar{\Omega} = 0 \quad \forall \delta u_r \in \mathbb{U}_r^0, \tag{29a}$$

$$\int_{\bar{\Omega}} \left[P_{zr}\frac{\partial \delta u_z}{\partial r} + P_{zz}\frac{\partial \delta u_z}{\partial z}\right] r \mathrm{d}\bar{\Omega} = 0 \quad \forall \delta u_z \in \mathbb{U}_z^0, \tag{29b}$$

$$\int_{\bar{\Omega}} \dot{\boldsymbol{\phi}} \delta p \, r \mathrm{d}\bar{\Omega} - \int_{\bar{\Omega}} \rho^{\mathrm{F}} \phi \left[W_r \frac{\partial \delta p}{\partial r} + W_z \frac{\partial \delta p}{\partial z}\right] r \mathrm{d}\bar{\Omega} = 0 \quad \forall \delta p \in \mathbb{P}^0. \tag{29c}$$

The appropriate trial and test sets are

$$\mathbb{U}_r = \left\{\boldsymbol{u}' \text{ suff. regular on } \bar{\Omega}\text{: } u' = 0 \text{ on } \bar{\Gamma}_{\mathrm{I}}\right\} = \mathbb{U}_r^0, \quad \text{smooth } \bar{\Gamma}_{\mathrm{T/B}}, \tag{30a}$$

$$\mathbb{U}_r = \left\{\boldsymbol{u}' \text{ suff. regular on } \bar{\Omega}\text{: } u' = 0 \text{ on } \bar{\Gamma}_{\mathrm{I}} \cup \bar{\Gamma}_{\mathrm{T/B}}\right\} = \mathbb{U}_r^0, \quad \text{rough } \bar{\Gamma}_{\mathrm{T/B}}, \tag{30b}$$

$$\mathbb{U}_z = \left\{\boldsymbol{u}' \text{ suff. regular on } \bar{\Omega}\text{: } u' = u^{\mathrm{T}}_{\mathrm{app}} \text{ on } \bar{\Gamma}_{\mathrm{T}}\right\}, \tag{30c}$$

$$\mathbb{U}_z^0 = \left\{\boldsymbol{u}' \text{ suff. regular on } \bar{\Omega}\text{: } u' = 0 \text{ on } \bar{\Gamma}_{\mathrm{T/B}}\right\}, \tag{30d}$$

$$\mathbb{P} = \left\{p' \text{ suff. regular: } p' = 0 \text{ on } \Gamma_{\mathrm{P}}\right\} = \mathbb{P}^0. \tag{30e}$$

Furthermore, we have introduced the internal (symmetry) boundary $\bar{\Gamma}_{\mathrm{I}}$ pertinent to axisymmetry.

For smooth boundary parts $\Gamma_{\mathrm{T/B}}$, we identify that the stress, fluid storage and seepage become uniform in the z direction. For the primal variables, we deduce that $\frac{\partial u_r}{\partial z} = \frac{\partial p}{\partial z} = 0$ and $u_z(r, z, t) = -\epsilon(t)z$, for the time-dependent compression, which results in $F = F(r, z)$ being uniform along z. Associated with this restrictions, we consider only test functions such that $\delta u_z = 0$ and $\frac{\partial \delta u_r}{\partial z} = \frac{\partial \delta p}{\partial z} = 0$. As a consequence, Eq. (29b) becomes obsolete while Eqs. (29a), (29c) are simplified and represent effectively a 1D-problem in $u_r(r, t)$, $p(r, t)$ for $r \in [0, R_0]$. Hence, the 1D problem to solve is: Find $(u_r, p) \in \mathbb{U} \times \mathbb{P}$ such that

$$\int_0^{R_0} \left[P_{rr}\frac{\partial \delta u_r}{\partial r} + P_{\theta\theta}\frac{1}{r}\delta u_r\right] r \, \mathrm{d}r = 0 \quad \forall \delta u_r \in \mathbb{U}^0, \tag{31a}$$

$$\int_0^{R_0} \dot{\boldsymbol{\phi}} \delta p \, r \mathrm{d}r - \int_0^{R_0} \rho^{\mathrm{F}} \phi \frac{\partial \delta p}{\partial r} W_r \, r \, \mathrm{d}r = 0 \quad \forall \delta p \in \mathbb{P}^0, \tag{31b}$$

where

$$\mathbb{U} = \left\{u' \text{ suff. regular on } [0, R_0] : \; u' = 0 \text{ at } r = 0\right\} = \mathbb{U}^0, \tag{32a}$$

$$\mathbb{P} = \left\{p' \text{ suff. regular on } [0, R_0] : \; p' = 0 \text{ at } r = R_0\right\} = \mathbb{P}^0. \tag{32b}$$

4.2. Parameter identification

To ensure that the model reliably represents the material behaviour, the parameters are calibrated against the experimental data. To this end, we introduce three different measures that are used for calibration

(i) The volume averaged normal stress:

$$\bar{P}_{zz}(t) := \frac{2}{R_0^2 H_0}\int_{\bar{\Omega}} P_{zz}(r, z, t) r \mathrm{d}\bar{\Omega}. \tag{33}$$

The average axial deformation gradient is

$$\bar{F}_{zz}(t) = \frac{2}{R_0^2 H_0}\int_{\bar{\Omega}} F_{zz}(r, z, t) \mathrm{d}\bar{\Omega} = 1 - \epsilon(t) \tag{34}$$

with $\epsilon(t) = -\frac{1}{H_0}u_{\mathrm{app}}(t)$. In order to obtain this result, it was used that $u_z(r, H_0, t) = u_{\mathrm{app}}(t)$ and $u_z(r, 0, t) = 0$. Clearly, $\epsilon(t)$ can be interpreted as the average axial compressive strain (negative elongation).

(ii) Diameter change at mid-height of the specimen:

$$\bar{d}(t) = \frac{1}{2R_0} 2u_r(R_0, \tfrac{1}{2}H_0, t), \tag{35}$$

(iii) Loss of pore fluid across the perimeter boundary $\bar{\Gamma}_{\mathrm{P}}$ during a given time interval $(0, T)$:

$$\bar{m}_{\mathrm{F}} = 2\pi R_0 \rho_0^{\mathrm{F}} \int_0^T \int_0^{H_0} \phi(R_0, z, t) W_{\mathrm{n}}(R_0, z, t) \mathrm{d}z \mathrm{d}t. \tag{36}$$

It is noted that $\rho^{\mathrm{F}} = \rho_0^{\mathrm{F}}$ for $r = R_0$ since $p = 0$ on $\bar{\Gamma}_{\mathrm{P}}$.

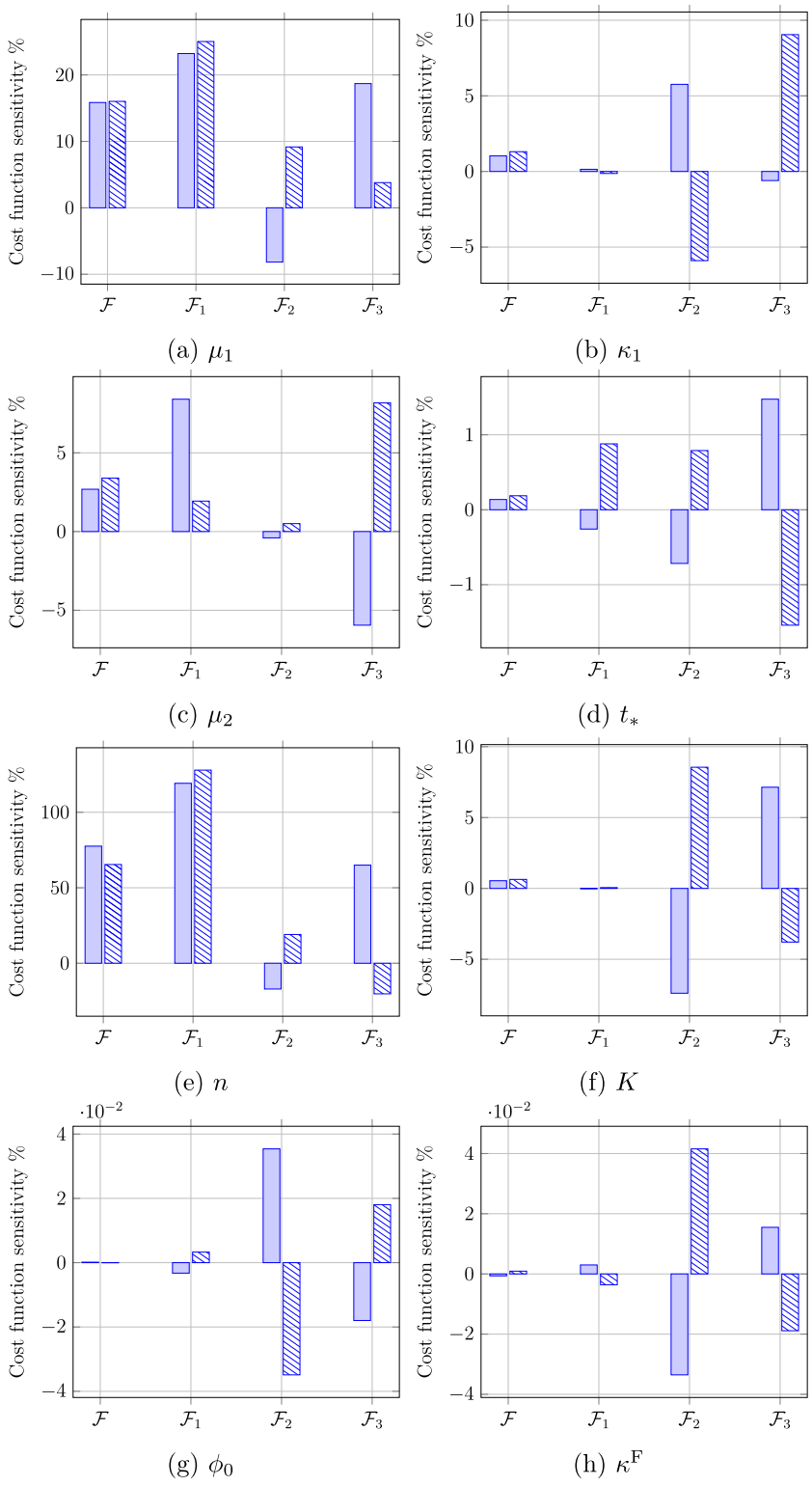

Fig. 4. Relative change of: the total cost function, $\mathcal{F}$, the cost term related to axial stress, $\mathcal{F}_1$, the cost term related to diameter evolution, $\mathcal{F}_2$, the cost term related to mass-loss, $\mathcal{F}_3$, as defined in Eq. (38). Sensitivities shown in (a) – (h) for a (▭): 10% increase and (▨): 10% decrease of the calibrated parameters shown in Table 1.

In total, nine parameters are to be determined. The first two parameters, μ_1 and κ_1, describe the elasto-static material response. Four parameters, μ_2, t_*, n, σ_0, govern the viscoelastic behaviour. The final three parameters, K, ϕ_0, and κ^{F} are fluid-related properties.

Furthermore, we note that the relaxation time and reference stress in Eq. (15) can be combined to a single parameter so that $A = t_*^{-1}\sigma_0^{-n}$. As a consequence, there exists infinite combinations of t_* and σ_0 that produce the same viscous response. For uniqueness, we choose $\sigma_0 = 10$ MPa and calibrate t_*. The complete parameter set is thus collected as the set

$$\boldsymbol{\theta} = \{\mu_1, \kappa_1, \mu_2, t_*, n, K, \phi_0, \kappa^{\mathrm{F}}\}. \tag{37}$$

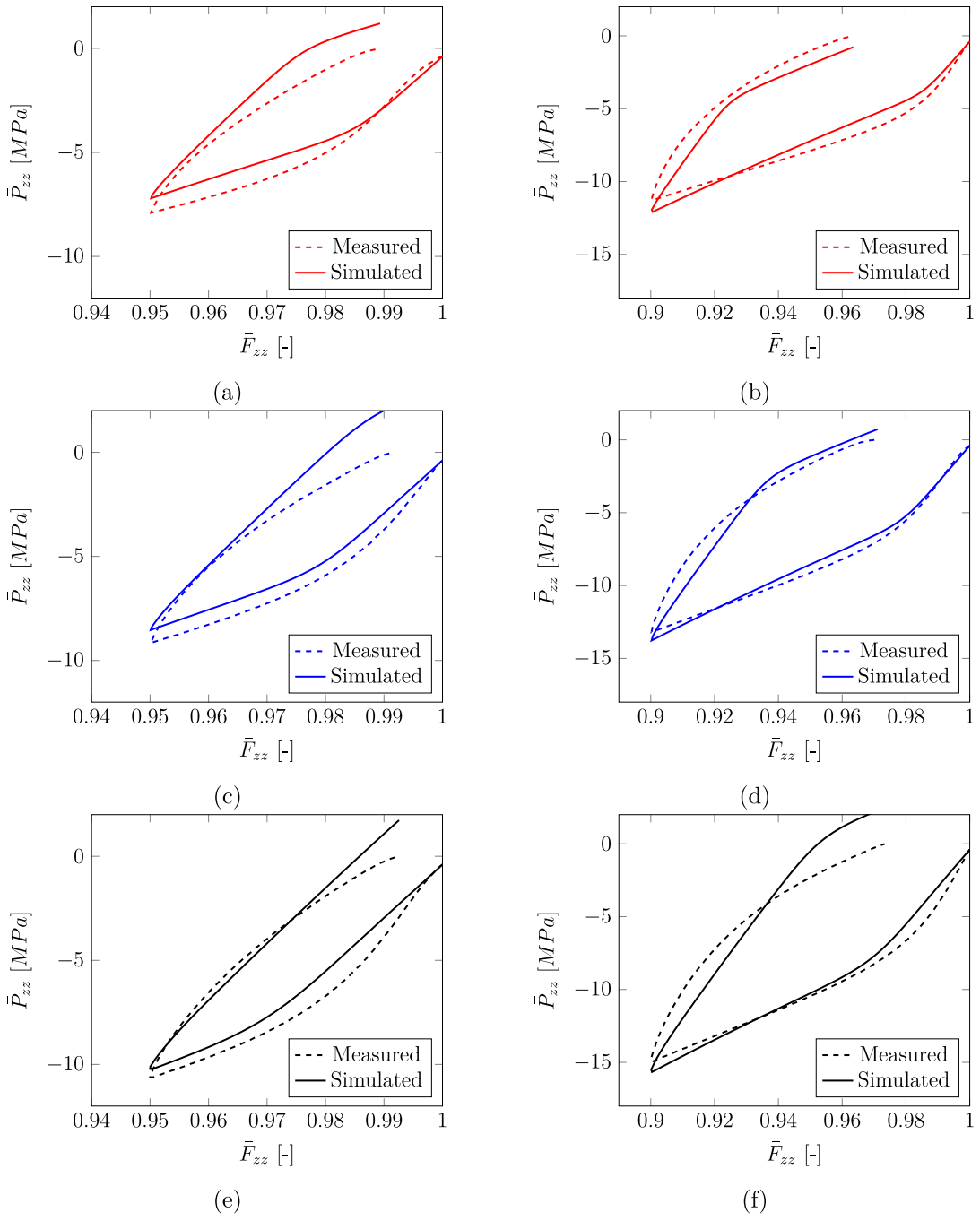

Fig. 5. Experimental and simulated compressive stress–strain responses for a smooth boundary $\Gamma_{\mathrm{T/B}}$ with a maximum deformation of 5% (a,c,e) and 10% (b,d,f). Results are shown for three different loading rates: (a, b) $\dot{\epsilon} = 0.1$ % / min. (c, d) $\dot{\epsilon} = 1$ % / min. (e, f) $\dot{\epsilon} = 10$ % / min.

The parameters should be chosen to minimize a cost function $\mathcal{F}$, which considers the difference between simulations and experiments for axial stresses, diameter evolution and loss of fluid mass, defined as

$$\mathcal{F}(\boldsymbol{\theta}, t) = \mathcal{F}_1 + \mathcal{F}_2 + \mathcal{F}_2, \tag{38a}$$

$$\mathcal{F}_1(\boldsymbol{\theta}, t) = \sum_{i=1}^{6} \left[P_{zz,i}^{\mathrm{exp}}(t) - \bar{P}_{zz,i}, (\boldsymbol{\theta}; t) \right]^2, \tag{38b}$$

$$\mathcal{F}_2(\boldsymbol{\theta}, t) = w_1 \sum_{j=1}^{3} \left[d_j^{\mathrm{exp}}(t) - \bar{d}_j(\boldsymbol{\theta}; t) \right]^2, \tag{38c}$$

$$\mathcal{F}_3(\boldsymbol{\theta}) = w_2 \sum_{i=1}^{6} \left[m_{\mathrm{F},i}^{\mathrm{exp}} - \bar{m}_{\mathrm{F},i}(\boldsymbol{\theta}) \right]^2. \tag{38d}$$

The first term related to axial stresses is denoted $\mathcal{F}_1$, the second term related to diameter evolution is denoted $\mathcal{F}_2$ and the third term for loss of fluid mass is denoted $\mathcal{F}_3$. Moreover, the weighting factors w_1 and w_2 are chosen such that the contributions of the three terms in Eq. (38a) are of similar magnitude.

4.3. Implementation

The proposed model is implemented in **COMSOL Multiphysics 6.2** using the *Mathematics* module. In particular, the *Weak Form PDE* interface is employed to directly input the space–time continuous formulations given in Eqs. (5a) and (5b). Time integration is carried out with the Backward Differentiation Formula (BDF) of order 1, equivalent to the backward Euler scheme. For the spatial discretization, a

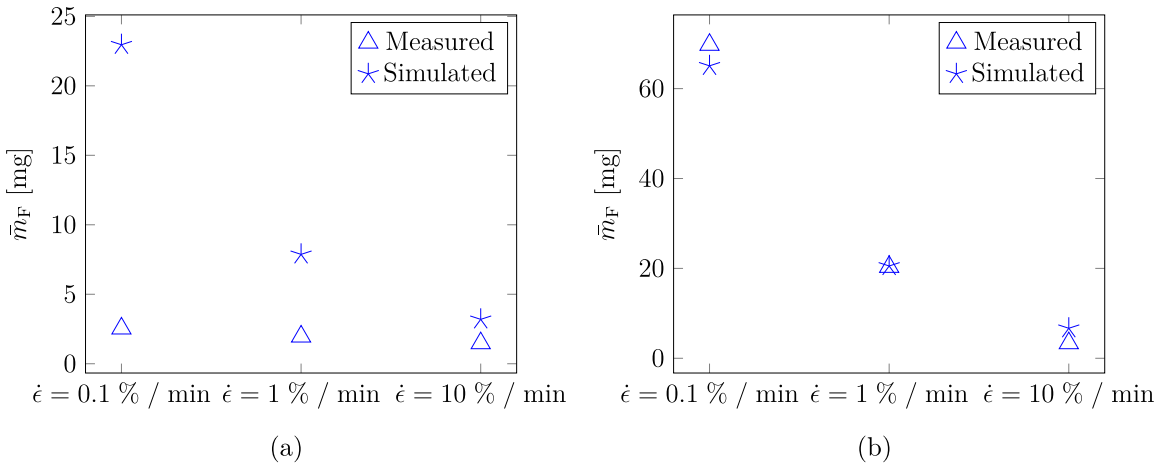

Fig. 6. Measured and simulated loss of fluid mass at: (a) 5% strain corresponding to Fig. 5a, c, e. (b) 10% strain corresponding to Fig. 5b, d, f.

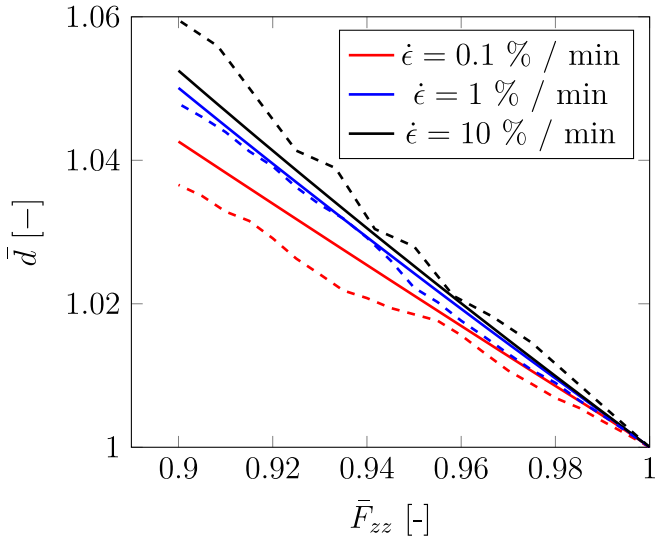

Fig. 7. Measured (dashed curves) and simulated (solid curves) diameter evolution against applied axial deformation.

quadratic approximation is employed for the displacement field, while the pore pressure field is discretized using linear shape functions. This choice corresponds to the well known Taylor Hood element, which satisfies the LBB condition and ensures numerical stability in the limit of small time steps (Taylor and Hood, 1973; Simo et al., 1985; Brezzi and Fortin, 2012). To perform parameter estimation, the COMSOL model is coupled with **MATLAB R2023b** via *LiveLink*, enabling external control of the optimization process. The calibration is performed using MATLAB's `fminsearch` routine, which implements the unconstrained Nelder–Mead simplex algorithm (Nelder and Mead, 1965).

For computational efficiency, we assume smooth boundaries that allow for one-dimensional specimen representation for model calibration, rather than the more computationally demanding rough boundaries that require a two-dimensional representation.

5. Results

The calibrated material parameters are presented in Table 1. The identified Norton exponent is relatively high, indicating a strongly stress sensitive viscous response that approaches perfectly plastic behaviour at high stress levels. The corresponding relaxation time reflects a comparatively stiff viscous branch; however, its absolute magnitude is not unique and depends on the choice of the reference stress used in the normalization of the evolution law in Eq. (15). The permeability is consistent with the expected pore size and porosity of the material, where larger pores and well connected pathways correspond to higher permeability, whereas fine and/or tortuous pore networks lead to lower values.

A sensitivity study of the cost function with respect to the calibrated parameters is shown in Fig. 4, where the parameters are perturbed one at a time by ±10 % of their calibrated value. The results suggest that a local minimum is obtained, as the total cost function $\mathcal{F}$ increases or remains unchanged under these perturbations. The sensitivity of the cost function is highest when perturbing the shear moduli μ_1 and μ_2 associated with the mechanical response, as well as the Norton exponent n, indicating that these parameters are strongly determined by the calibration data. In contrast, parameters exhibiting low sensitivity may be varied in their calibrated values, as variations in these parameters have only a minor effect on the cost function.

The compressive stress–strain responses obtained from experimental tests, along with the simulated average compressive stress computed using Eq. (33), are presented in Fig. 5 for the case of a smooth boundary $\Gamma_{T/B}$. For all cases, the stress–strain behaviour is distinctly nonlinear during both loading and unloading. The loading paths exhibit an initial steep increase in stress, followed by a gradual reduction in stiffness with increasing strain, indicative of material softening. The unloading curves are also nonlinear and do not simply retrace the loading trajectories. Instead, they form pronounced hysteresis loops that reflect energy dissipation during each loading cycle. The size of these loops appears to depend primarily on the strain magnitude rather than the strain rate, and residual strain is consistently observed upon unloading to zero stress. However, this residual deformation gradually relaxes over time, suggesting that the overall material response remains elastic.

Fig. 5a and 5b show the 1st PK stress during loading up to $\epsilon = 5$ % and $\epsilon = 10$ %, and the subsequent unloading, both at the low rate of $\dot{\epsilon} = 0.1$ % / min. At this rate, both the experimental and simulated stress magnitudes are the lowest, and the response is accompanied by substantial fluid seepage, see Fig. 12a. This behaviour indicates that solid–fluid interaction is small and that the solid skeleton carries the major part of the mechanical load. The model predictions capture well the overall nonlinear shape of the response, including the softening behaviour and the unloading path, although minor deviations are observed at large strain levels.

Fig. 5c and 5d illustrate the material response at the intermediate rate of $\dot{\epsilon} = 1$ % / min. At this loading rate, the stress magnitudes, as well as the initial stiffness, are noticeably higher compared with the 0.1% / min rate. Fluid seepage is significantly reduced, as seen in Fig. 12b, indicating that the pressurized fluid begins to interact more strongly

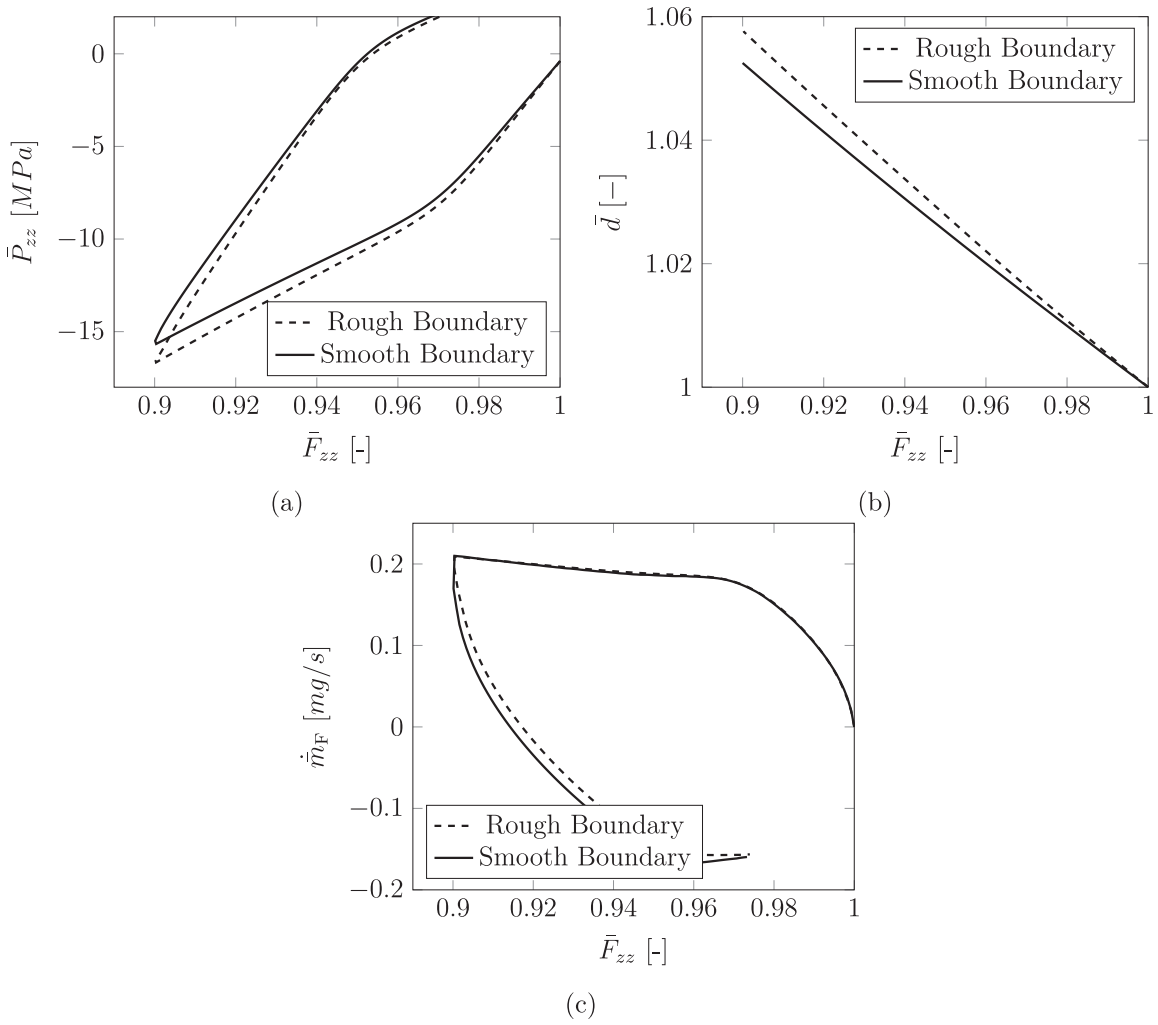

Fig. 8. Comparison of the smooth and rough boundaries at a strain rate of 10% per minute: (a) The simulated average axial loading-unloading stress. (b) Diameter evolution of the specimen. (c) Rate of fluid mass loss as a function of applied axial deformation.

Table 1
Table of material parameters.

Parameters	Description	Value	Source	Eq.
μ_1	Static shear modulus	29.0 MPa	Calibrated	(11)
κ_1	Static bulk modulus	63.2 MPa	Calibrated	(11)
μ_2	Dynamic shear modulus	55.7 MPa	Calibrated	(12)
t_*	Relaxation time	8.66 s	Calibrated	(15)
n	Norton exponent	6.18	Calibrated	(15)
σ_0	Reference stress	10 MPa	Assumed	(15)
K	Permeability	$7.77 \cdot 10^{-18}$ m^2	Calibrated, (Carlstedt et al., 2022)	(21)
ϕ_0	Initial porosity	0.21	Calibrated, Duan et al. (2023), Carlstedt et al. (2022)	(19)
κ^F	Fluid bulk modulus	3.95 GPa	Calibrated, Wang et al. (2023)	(20)
ρ_0^F	Initial fluid density	1.35 g/cm^3	Canrud (2025)	(20)

with the solid phase and contribute to the load bearing response. The model reproduces the experimental data well, in particular for the 10% strain level in Fig. 5d. In Fig. 5c, the initial stiffness is slightly underestimated.

At the high rate, $\dot{\epsilon}$ = 10 % / min, the specimens exhibit even larger stress magnitudes and stiffness, as shown in Fig. 5e and 5f. No fluid seepage is visually detected under this condition, as shown in Fig. 12c, indicating that the fluid phase is effectively trapped and the solid–fluid interaction is maximized. The model predictions align well with the experimental results at the high rate.

Fig. 6a and 6b compare the measured and simulated loss of fluid mass, $\bar{m}_F$, that is computed using Eq. (36). The measurements were conducted at the end of each unloading cycle, i.e., at zero stress in Fig. 5, providing one data point for each strain rate and strain level. At 5 % compressive strain in Fig. 6a, the measured mass loss is small, almost negligible, for all loading rates. In contrast, significant mass loss is observed at 10 % compressive strain shown in Fig. 6b, in particular for the slow and intermediate rates. This is consistent with the images presented in Fig. 12. At this strain level, more than 60 mg of liquid electrolyte is lost at the lowest rate $\dot{\epsilon}$ = 0.1 % / min, and the measured loss of mass decreases progressively with increasing loading rate. The model overestimates the loss of mass at 5 % strain shown in Fig. 6a; however, it is able to predict the loss of mass at 10 % strain in Fig. 6b with high accuracy.

Fig. 7 presents the measured diameter change versus applied axial deformation, together with the corresponding model predictions

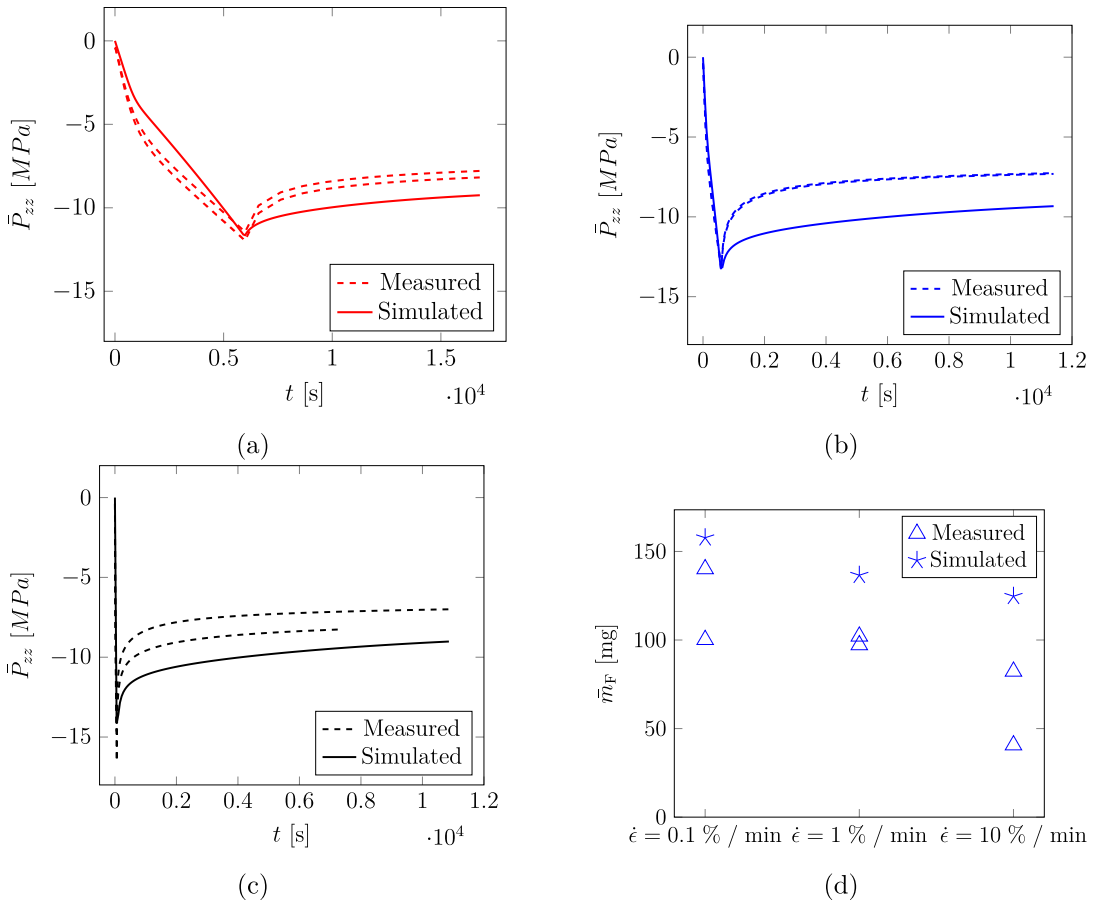

Fig. 9. Experimental and simulated stress relaxation versus time. The specimens are compressed to 10 % strain and held at the current strain level over time. Two specimens were subjected to stress relaxation testing per loading rate: (a) $\dot{\epsilon}$ = 0.1 % / min. (b) $\dot{\epsilon}$ = 1 % / min. (c) $\dot{\epsilon}$ = 10 % / min. (d) Measured and simulated loss of fluid mass, as shown in (a)–(c).

computed using Eq. (35) for all considered loading rates. The results indicate a clear rate dependence on the diameter evolution, with higher rates leading to greater radial expansion. At the highest loading rate, noticeable barrelling of the cylindrical specimen is observed, see Fig. 12c. The calibrated model successfully reproduce the experimental observations with good agreement. It should be noted that the measurements were obtained using an optical camera and are, therefore, subject to considerable uncertainty.

Furthermore, Fig. 8 compares the obtained simulation results for smooth and rough boundaries, as described in Section 3.2. In this analysis, the highest strain rate of $\dot{\epsilon}$ = 10 % / min is considered to maximize the fluid–solid interaction. Fig. 8a presents the simulated average axial stress response for an applied axial strain of 10 %. It is found that the rough boundaries produce a slightly stiffer response than the smooth boundaries. We emphasize that the actual experimental situation lies between the extreme conditions of smooth and rough boundaries. No separate measurement was made to quantify the friction coefficient, however the pronounced barelling, cf. Fig. 12c, that was recorded for the highest strain rate (close to undrained condition) indicates that friction is significant. We thus conjecture that the rough conditions is closer to reality than the smooth conditions.

At small deformations, the simulated diameter evolution is nearly identical for both smooth and rough boundaries in Fig. 8b. However, with increasing axial strain, the simulated diameter evolution at the mid-height of the specimen for assumed rough boundaries is shown to increase progressively due to the development of barrelling.

Finally, Fig. 8c shows the rate of fluid mass loss $\dot{m}_F$ as a function of applied axial deformation. The results indicate a seepage profile for rough boundaries that is similar to smooth ones, since integration of the profiles using Eq. (36) yields essentially the same total volume loss. Furthermore, we note that the model produces a negative mass flux during the unloading of the specimen. A negative flux means that the fluid flow is reversed and that some the leaked fluid returns to the specimen. The adopted boundary condition of zero pressure allows for the fluid to re-enter the specimen during unloading. This reversed flow is not observed experimentally and is merely an artifact of the chosen Dirichlet boundary condition. The radial displacement and pore pressure fields at 10% strain are presented in Fig. 13.

Fig. 9 presents the results of the relaxation tests described in Section 2.4. We emphasize that these test data are used solely for model validation, i.e., the model was not calibrated to fit any results from the relaxation tests.

Fig. 9a – c show how the experimental and simulated axial compressive stress responses evolve with time during and after loading with different rates. During loading, the stress evolution resembles that observed in Fig. 5, beginning with an initial linear region followed by a gradual softening of the stiffness. Once the axial strain reaches 10 %, the specimens are held at this constant deformation level.

In Fig. 9a, a sharp stress drop is observed during the transition from loading to holding, followed by gradual nonlinear relaxation over time. Upon comparing the relaxation plots in Fig. 9a – c, we note that the magnitude of the stress drop is rate dependent, where the highest rate in Fig. 9c, shows the most pronounced drop. After sufficient time has elapsed, the stress in all cases relaxes to an equilibrium value of approximately 7 MPa.

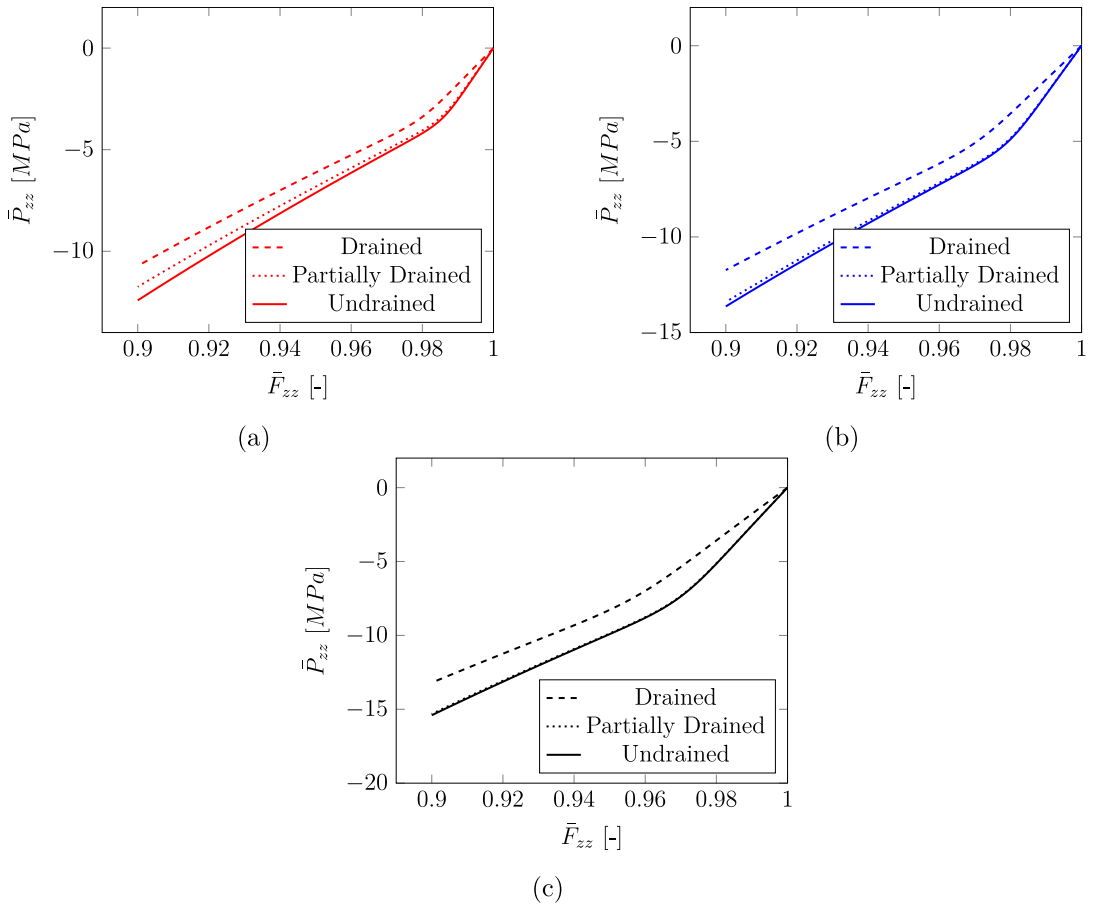

Fig. 10. Simulated drained, undrained and partially drained stress–strain responses at a state of uniaxial stress: (a) $\dot{\epsilon}$ = 0.1 % / min. (b) $\dot{\epsilon}$ = 1 % / min. (c) $\dot{\epsilon}$ = 10 % / min.

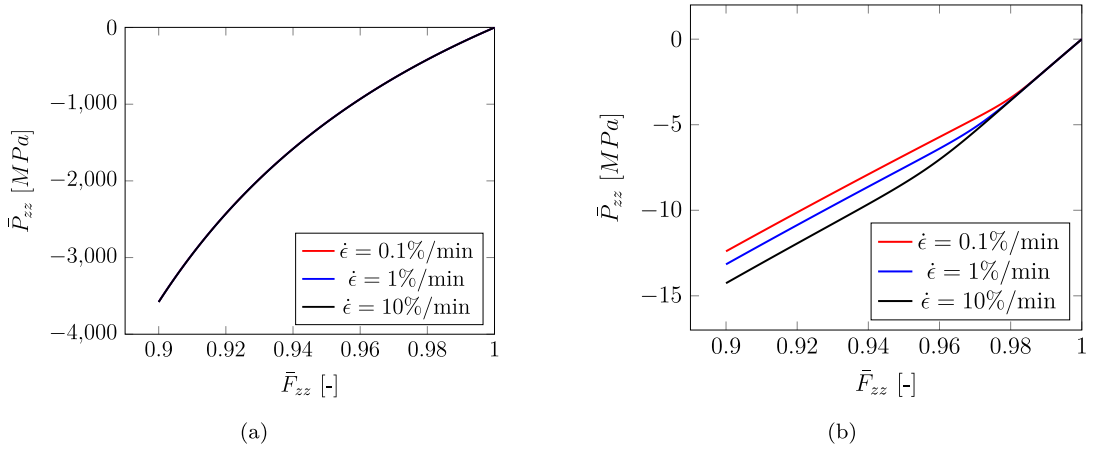

Fig. 11. Simulated rate-dependent response at a state of uniaxial strain. (a) Undrained condition. (b) Drained condition.

Fig. 9d shows the corresponding measurements of loss of fluid mass after relaxation. Here, we obtain two data points per load rate, corresponding to two stress relaxation tests per load rate. The greatest mass loss is observed for the low rate $\dot{\epsilon}$ = 0.1 % / min, consistent with the substantial fluid seepage observed under slow loading conditions. Although additional seepage and stress reduction are expected over longer times, the samples had not yet reached equilibrium at the end of the test, suggesting that further minor relaxation and mass loss would occur over time.

The model predictions show overall fair agreement with the experiments, with the maximum stress accurately captured across loading rates in Fig. 9. However, the magnitude of the stress drop and the subsequent relaxation during the hold phase are consistently underestimated. This discrepancy is likely due to limitations in the constitutive and transport assumptions of the model. Although increasing permeability improves the predicted stress relaxation, it leads to poorer agreement with the measured mass loss, which is included in the cost function. We note that additional mechanisms such as deformation dependent

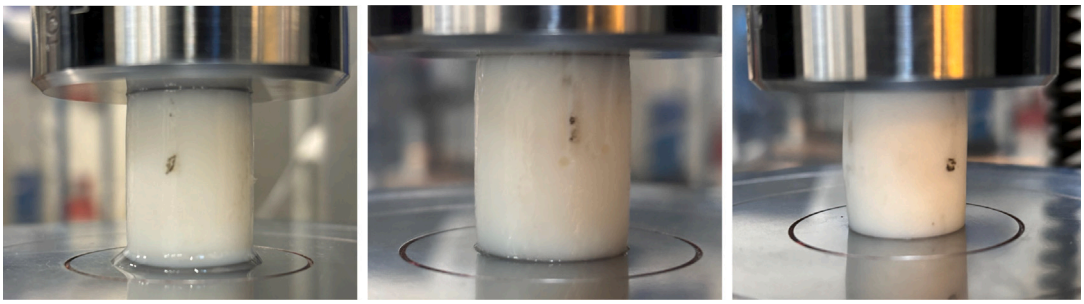

Fig. 12. (a) Pictures of cylindrical specimens subjected to 10% compressive strain at: (a) $\dot{\epsilon} = 0.1$ % / min. (b) $\dot{\epsilon} = 1$ % / min. (c) $\dot{\epsilon} = 10$ % / min.

permeability cf. Rollin et al. (2025), are omitted in the modelling framework, since their individual roles cannot be uniquely identified within the present experimental setup. Incorporating more viscoelastic branches in the modelling approach and a more advanced seepage description is therefore expected to improve predictions in future work.

Fig. 10 shows the simulated average axial stress during compressive loading up to ϵ =10 %. Here, we explore the bounds within which the calibrated model operates. The lower bound is represented by the *drained* solid skeleton, which is obtained if we set $p = 0$ everywhere in the specimen. Conversely, the upper bound corresponds to the *undrained* condition, which is obtained if the permeability is zero (corresponding to $\boldsymbol{W} = \boldsymbol{0}$) in the entire specimen. What remains of the continuity equation is only the storage term. Both the drained and undrained cases result in completely homogeneous pore pressure and displacement fields if we choose a smooth $\Gamma_{\mathrm{T/B}}$. In practice, this means that the computations can be carried out at the constitutive level. These extreme situations are contrasted to the general situation with inhomogeneous pore pressure (and drainage) in the specimen, whereby we choose a smooth boundary $\Gamma_{\mathrm{T/B}}$.

The first series of results (in Fig. 10a – c) were obtained for different loading rates $\dot{\epsilon}$, while a state of uniaxial stress is ensured. Fig. 10a presents the simulation results for $\dot{\epsilon} = 0.1$ % per minute. The predicted response of the partially drained model lies between the drained and undrained bounds, initially slightly skewed towards the undrained response. For intermediate and high loading rates, $\dot{\epsilon} = 1$ % and $\dot{\epsilon} = 10$ % / min in Fig. 10b and 10c, the partially drained responses shift closer to the undrained, indicating that fluid mobility decreases as the deformation rate increases.

The next series of results (in Fig. 11a – b) concern the response under uniaxial strain, which is simulated on the "constitutive level". Fig. 11a shows the simulated undrained response for all different strain rates $\dot{\epsilon}$. Since the material point is constrained to deform only in the axial direction, this results in a progressive increase in axial stress and a maximized fluid–solid interaction. Fig. 11b, in contrast, shows the undrained response. It is concluded that the magnitude of stress increases with increasing $\dot{\epsilon}$, while the initial stiffness remains rate-independent. These findings indicate that the presence of the confined fluid may induce pronounced stress concentrations within the material under uniaxial strain conditions. Furthermore, for the considered range of loading rates, the partially drained model predictions tend to align more closely with the undrained bound than with the drained bound.

6. Conclusions and outlook

We show that modelling of the structural battery electrolyte subjected to compressive loading requires a poro-viscoelastic representation to capture observed deformations and electrolyte seepage. This is to the authors knowledge, the first ever attempt to model and calibrate the SBE material in a non-linear setting with poro-viscoelastic characteristics. With such a computational model, we successfully reproduce the compressive stress–strain behaviour observed experimentally at different rates of loading. Specifically, the model captures the increased sample barrelling and decreased electrolyte mass loss with increased axial loading rate, in particular at higher compressive deformation. By exploring the drained and undrained bounds, we demonstrate that the adoption of a porous media model is essential for accurate stress predictions, as current model predictions lie close to the undrained bound.

As to future work, it would be beneficial to have access to experimental data on the pore pressure distribution in the entire sample (to be used for calibration and/or validation). The adopted version of Darcy-type seepage is certainly simplistic, cf., the philosophy behind the St. Venant model for hyperelasticity. By introducing accurate experimental data for pore pressure, further refinement of the seepage model can be made to improve material relaxation predictions. This work establishes a framework for calibration of compression and relaxation behaviour, whereas the response under repeated mechanical and electrochemical cycling remains to be investigated.

CRediT authorship contribution statement

Carl Larsson: Writing – review & editing, Writing – original draft, Visualization, Software, Methodology, Investigation, Formal analysis, Conceptualization. **Fredrik Larsson:** Writing – review & editing, Writing – original draft, Supervision, Methodology, Investigation, Conceptualization. **Ruben Tavano:** Writing – original draft, Resources, Investigation. **Johanna Xu:** Writing – review & editing, Supervision, Resources, Methodology, Investigation. **Kenneth Runesson:** Writing – review & editing, Writing – original draft, Methodology. **Leif E. Asp:** Writing – review & editing, Writing – original draft, Supervision, Project administration, Methodology, Conceptualization.

Declaration of competing interest

The authors declare that they have no known competing financial interests or personal relationships that could have appeared to influence the work reported in this paper.

Acknowledgements

The project is funded by the USAF via the EOARD, USA Award No. FA8655-25-1-7049, ONR, USA, Award No. N62909-22-1-2037, Swedish Research Council, grant number 2020-05057, and 2D TECH VINNOVA competence Center, Sweden, grant number 2019-00068.

Data availability

Data will be made available on request.

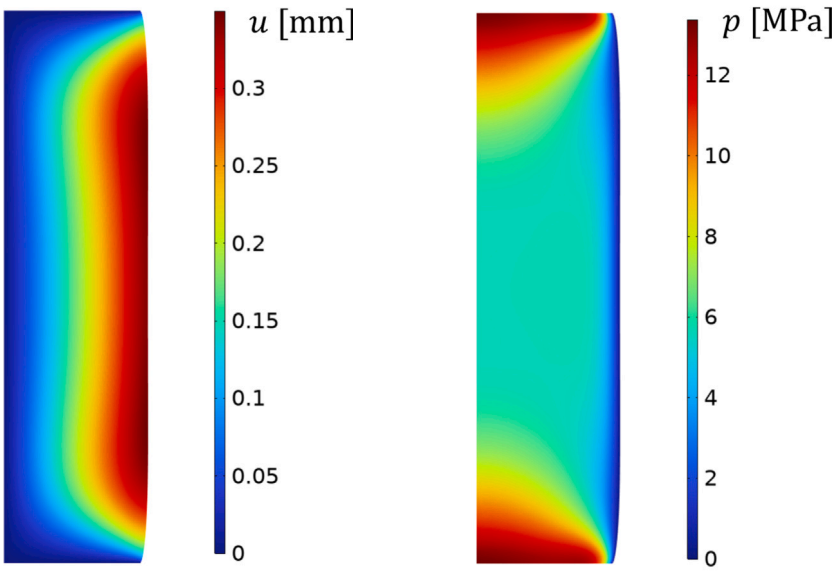

Fig. 13. Simulation results for a rough top boundary: (a) Displacement field at 10% compressive strain for the loading rate $\dot{\epsilon}$ = 10 % / min. (b) Pore pressure field at 10% compressive strain for the loading rate $\dot{\epsilon}$ = 10 % / min.

References

Brezzi, F., Fortin, M., 2012. Mixed and Hybrid Finite Element Methods, vol. 15, Springer Science & Business Media.

Canrud, 2025. URL https://www.canrud.com/products/detail/2840. (Accessed on 14 October 2025).

Carlstedt, D., Runesson, K., Larsson, F., Jänicke, R., Asp, L.E., 2023. Variationally consistent modeling of a sensor-actuator based on shape-morphing from electro-chemical–mechanical interactions. J. Mech. Phys. Solids 179, 105371. http://dx.doi.org/10.1016/j.jmps.2023.105371.

Carlstedt, D., Runesson, K., Larsson, F., Tu, V., Jänicke, R., Asp, L.E., 2022. Computational modelling of structural batteries accounting for stress-assisted convection in the electrolyte. Int. J. Solids Struct. 238, 111343. http://dx.doi.org/10.1016/j.ijsolstr.2021.111343.

Cattaruzza, M., Fang, Y., Furó, I., Lindbergh, G., Liu, F., Johansson, M., 2023. Hybrid polymer-liquid lithium ion electrolytes: effect of porosity on the ionic and molecular mobility. J. Mater. Chem. A 11, 7006–7015. http://dx.doi.org/10.1039/D3TA00250K.

Chaudhary, R., Xu, J., Xia, Z., Asp, L.E., 2024. Unveiling the multifunctional carbon fiber structural battery (adv. mater. 48/2024). Adv. Mater. 36 (48), 2470382. http://dx.doi.org/10.1002/adma.202470382.

De Boer, R., 2012. Theory of Porous Media: Highlights in Historical Development and Current State. Springer Science & Business Media.

Duan, S., Cattaruzza, M., Tu, V., Auenhammer, R.M., Jänicke, R., Johansson, M.K.G., Liu, F., Asp, L.E., 2023. Three-dimensional reconstruction and computational analysis of a structural battery composite electrolyte. Commun. Mater. 4, 49. http://dx.doi.org/10.1038/s43246-023-00377-0.

Duan, S., Iyer, A.H., Carlstedt, D., Rittweger, F., Sharits, A., Maddox, C., Riemschneider, K.-R., Mollenhauer, D., Colliander, M., Liu, F., Asp, L.E., 2021. Effect of lithiation on the elastic moduli of carbon fibres. Carbon 185, 234–241. http://dx.doi.org/10.1016/j.carbon.2021.09.037.

Ehlers, W., 2018. Effective stresses in multiphasic porous media: A thermodynamic investigation of a fully non-linear model with compressible and incompressible constituents. Geomech. Energy Environ. 15, 35–46. http://dx.doi.org/10.1016/j.gete.2017.11.004.

Ehlers, W., Markert, B., 2001. A linear viscoelastic biphasic model for soft tissues based on the theory of porous media. J. Biomech. Eng. 123 (5), 418–424. http://dx.doi.org/10.1115/1.1388292.

Ihrner, N., Johannisson, W., Sieland, F., Zenkert, D., Johansson, M., 2017. Structural lithium ion battery electrolytes via reaction induced phase-separation. J. Mater. Chem. A 5 (48), 25652–25659. http://dx.doi.org/10.1039/C7TA04684G.

Johannisson, W., Harnden, R., Zenkert, D., Lindbergh, G., 2020. Shape-morphing carbon fiber composite using electrochemical actuation. Proc. Natl. Acad. Sci. 117 (14), 7658–7664. http://dx.doi.org/10.1073/pnas.1921132117.

Larsson, C., Larsson, F., Xu, J., Runesson, K., Asp, L.E., 2023. Effects of lithium insertion induced swelling of a structural battery negative electrode. Compos. Sci. Technol. 244, 110299. http://dx.doi.org/10.1016/j.compscitech.2023.110299.

Larsson, C., Larsson, F., Xu, J., Runesson, K., Asp, L.E., 2025. Electro-chemo-mechanical modelling of structural battery composite full cells. Npj Comput. Mater. 11 (1), 141. http://dx.doi.org/10.1038/s41524-025-01646-x.

Nelder, J.A., Mead, R., 1965. A simplex method for function minimization. Comput. J. 7 (4), 308–313. http://dx.doi.org/10.1093/comjnl/7.4.308.

Pipertzis, A., Abdou, N., Xu, J., Asp, L.E., Martinelli, A., Swenson, J., 2023. Ion transport, mechanical properties and relaxation dynamics in structural battery electrolytes consisting of an imidazolium protic ionic liquid confined into a methacrylate polymer. Energy Mater. 3 (6), http://dx.doi.org/10.20517/energymater.2023.49.

Pipertzis, A., Xu, J., Abdou, N., Martinelli, A., Asp, L., Swenson, J., 2025. Ionic and electronic conductivity in structural negative electrodes. Electrochim. Acta 512, 145501. http://dx.doi.org/10.1016/j.electacta.2024.145501.

Reese, S., Govindjee, S., 1998. A theory of finite viscoelasticity and numerical aspects. Int. J. Solids Struct. 35 (26), 3455–3482. http://dx.doi.org/10.1016/S0020-7683(97)00217-5.

Rollin, D.R., Larsson, F., Runesson, K., Jänicke, R., 2025. Deformation dependent permeability from variationally consistent homogenization. GAMM-Mitt. 48 (4), e70010. http://dx.doi.org/10.1002/gamm.70010.

Sanavia, L., Schrefler, B., Steinmann, P., 2002. A formulation for an unsaturated porous medium undergoing large inelastic strains. Comput. Mech. 28 (2), 137–151. http://dx.doi.org/10.1007/s00466-001-0277-8.

Schneider, L.M., Ihrner, N., Zenkert, D., Johansson, M., 2019. Bicontinuous electrolytes via thermally initiated polymerization for structural lithium ion batteries. ACS Appl. Energy Mater. 2, 4362–4369. http://dx.doi.org/10.1021/acsaem.9b00563.

Schrefler, B., 2002. Mechanics and thermodynamics of saturated/unsaturated porous materials and quantitative solutions*. Appl. Mech. Rev. 55 (4), 351–388. http://dx.doi.org/10.1115/1.1484107.

Simo, J., Taylor, R., Pister, K., 1985. Variational and projection methods for the volume constraint in finite deformation elasto-plasticity. Comput. Methods Appl. Mech. Engrg. 51 (1), 177–208. http://dx.doi.org/10.1016/0045-7825(85)90033-7.

Tavano, R., Spagnol, M., Al-Ramahi, N., Joffe, R., Xu, J., Asp, L.E., 2024. Mechanical characterisation of a structural battery electrolyte. Polymer 312, 127646. http://dx.doi.org/10.1016/j.polymer.2024.127646.

Taylor, C., Hood, P., 1973. A numerical solution of the Navier-Stokes equations using the finite element technique. Comput. & Fluids 1 (1), 73–100. http://dx.doi.org/10.1016/0045-7930(73)90027-3.

Terzaghi, K., Peck, R.B., Mesri, G., 1996. Soil Mechanics in Engineering Practice. John wiley & sons.

Tu, V., Asp, L.E., Shirshova, N., Larsson, F., Runesson, K., Jänicke, R., 2020. Performance of bicontinuous structural electrolytes. Multifunct. Mater. 3 (2), 025001. http://dx.doi.org/10.1088/2399-7532/ab8d9b.

Wang, A.A., Persa, D., Helin, S., Smith, K.P., Raymond, J.L., Monroe, C.W., 2023. Compressibility of lithium hexafluorophosphate solutions in two carbonate solvents. J. Chem. Eng. Data 68 (4), 805–812. http://dx.doi.org/10.1021/acs.jced.2c00711.